Journal of Structural Geology 32 (2010) 766–780

Contents lists available at ScienceDirect

Journal of Structural Geology

journal homepage: www.elsevier.com/locate/jsg

Controls on fault damage zone width, structure, and symmetry in the Bandelier Tuff, New Mexico

Paul R. Riley [a,*], Laurel B. Goodwin [a], Claudia J. Lewis [b]

[a] University of Wisconsin-Madison, 1215 W. Dayton St., Madison, WI 53706, USA
[b] Los Alamos National Laboratory, EES-13, MS D452 Los Alamos, NM 875445, USA

ARTICLE INFO

Article history:
Received 10 March 2009
Received in revised form
1 May 2010
Accepted 12 May 2010
Available online 20 May 2010

Keywords:
Fault zone
Rio Grande rift
Damage zone
Fracture density
Bandelier Tuff

ABSTRACT

We studied welded and glassy nonwelded ignimbrites of the Bandelier Tuff cut by the Pajarito fault system to examine the influence of primary lithology and structure on fault damage-zone characteristics. Our work supports previous studies that indicate welding and resulting rock strength are first-order controls on the type of fault-zone structure that forms in high porosity ignimbrites. However, inherited mechanical anisotropy is the most significant control on spatial variations in fault-zone width and orientation of structures for a given throw. Cooling joints in welded ignimbrite localize strain, producing a narrower damage zone than that in glassy nonwelded ignimbrite. The joints also control the orientations of discrete fractures formed during faulting, so fractures show the same patterns inside and outside damage zones, which we attribute to local reorientation of stresses adjacent to joints. In contrast, deformation bands formed in relatively isotropic, glassy nonwelded ignimbrite exhibit conjugate sets oblique to the Pajarito fault, consistent with left-lateral extension across a pre-existing structure. Where footwall and hanging wall damage-zone widths can be compared in welded ignimbrite, they reflect greater hanging wall deformation, consistent with near-surface faulting. These observations collectively record 3D strain of a physically heterogeneous system.

1. Introduction

Upper crustal faults are most accurately described as 3-D volumes rather than 2-D surfaces. Within these volumes, the majority of slip accumulates within a fault core, which is surrounded by a less deformed damage zone (e.g., Chester et al., 1993; Caine et al., 1996; Shipton et al., 2006). The implications of this architecture are diverse. For example, fault-related deformation can change rock mechanical properties (Faulkner et al., 2008), causing stress orientations to rotate in fault damage zones, and affecting seismicity over time (Faulkner et al., 2006). The types, densities, and orientations of structures in fault zones also exert a first-order control on fault-zone permeability structure, permeability anisotropy, and flow pathways (e.g., Knipe, 1993; Haneberg, 1995; Caine et al., 1996; Zhang and Sanderson, 1995; Rawling et al., 2001).

Rawling et al. (2001) suggested that understanding petrophysical controls on fault-zone deformation processes could facilitate prediction of fault-zone structure from knowledge of faulted materials; i.e., faults in granite develop different structures than faults in poorly lithified sediments. Likewise, the addition of clay to sandstone results in narrower deformation band fault zones (Antonellini and Aydin, 1995), and large-displacement fault zones in poorly lithified clastic sediments are narrowest where numerous juxtaposed clay layers are present, and are widest where juxtaposed beds are sand and gravel (Heynekamp et al., 1999; Minor and Hudson, 2007). Similarly, Shipton et al. (2006) proposed that lithologic controls may affect the degree to which damage zone width increases with displacement.

To further explore the effects of lithology on damage zone evolution in normal faults, we have documented variations in damage zone structure and width of the Pajarito fault system in the 1.6–1.2 Ma Bandelier Tuff of New Mexico (Smith and Bailey, 1966; Izett and Obradovich, 1994; Fig. 1). Earlier work identified a mechanical stratigraphy within the ignimbrites that compose the Bandelier Tuff. Glassy nonwelded ignimbrites in which volcanic clasts are not fused together form deformation bands, whereas ignimbrites in which clasts are welded exhibit extensive damage-zone fractures (Wilson et al., 2003) (Fig. 2).

The Pajarito fault system is seismically active, with numerous fault scarps across which throw has been well documented (Lewis et al., 2009). In addition, the exposures we studied have been above the water table since deposition, such that variations in pore fluid

* Corresponding author. Tel.: +1 608 262 8960; fax: +1 608 262 0693.
E-mail address: priley@geology.wisc.edu (P.R. Riley).

0191-8141/$ – see front matter © 2010 Elsevier Ltd. All rights reserved.
doi:10.1016/j.jsg.2010.05.005

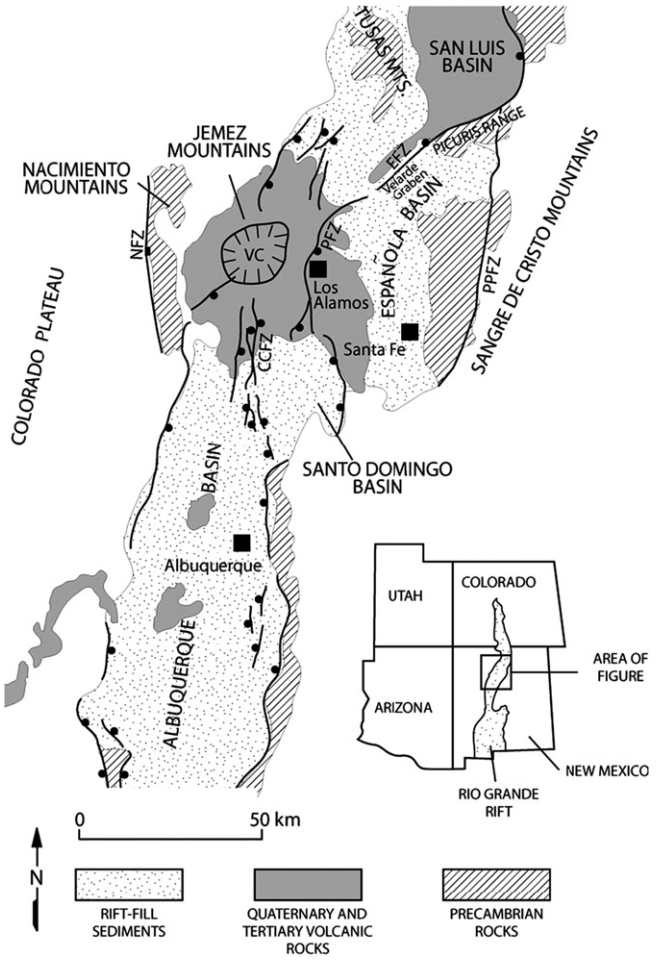

Fig. 1. The Rio Grande rift in north-central New Mexico. Basins and associated normal faults trend north to northeast. Box indicates location of Fig. 2. VC – Valles Caldera, PFZ – Pajarito fault zone, EFZ – Embudo fault zone, and CCFZ – Cañada del Cochiti fault zone. Modified from Gardner and Goff (1984) and Broxton and Vaniman (2005).

pressure cannot have played a role in deformation. Thus, we have examined the effect of the same deformation, at the same conditions of pressure, temperature, and pore fluid pressure, on mechanically distinct units, so the structures should reflect the influence of mechanical variation alone. We use these data to evaluate:

(1) the nature of lithologic controls on damage zone structure,
(2) potential lithologic and primary structural controls on damage zone width,
(3) lithologic controls on spacing of damage zone structures, and
(4) symmetry of fault-zone architecture.

2. Geologic setting

The Pajarito fault zone is a tectonically active, northerly trending normal fault zone that bounds the western side of the Española Basin of the Rio Grande rift (Fig. 1) (Kelley, 1979; Baldridge et al., 1995; Wolff and Gardner, 1995; Gardner et al., 1999, 2001). The Pajarito fault, a steeply east-dipping normal fault, dominates the fault zone, with maximum surface displacement of over 120 m on the central portion of the fault (Fig. 2) (e.g., Lewis et al., 2009). The fault zone consists of a series of mechanically linked segments in the north (e.g., Rendija Canyon and Guaje Mt. faults; Lewis et al., 2009); and in the south, it tips out along one main segment. Associated with the major faults that constitute the fault system are numerous small-scale faults and fractures that have been documented within the Bandelier Tuff (Carter and Winter, 1995; Gardner et al., 1999; Wilson et al., 2003; Wilson, 2004).

The Bandelier Tuff comprises a series of ignimbrite deposits erupted from the Toledo and Valles calderas, and is the primary stratigraphic unit that forms the Pajarito Plateau (Smith and Bailey, 1966; Gardner and Goff, 1984). It includes two members, the 1.6 Ma Otowi Member (Qbo) and the 1.2 Ma Tshirege Member (Qbt) (Fig. 3; Izett and Obradovich, 1994). They are primarily composed of silicic ash with varying amounts of pumice, lithic fragments, and phenocrysts (Broxton et al., 1995; Gardner et al., 1999; Wilson et al., 2003). Separating the Tshirege Member from the Otowi Member is the 1.6–1.3 Ma Cerro Toledo interval (Qct), a reworked rhyolitic volcaniclastic unit erupted from domes within the Toledo Caldera (Fig. 3) (Smith et al., 1970; Spell et al., 1996).

The Bandelier Tuff includes both nonwelded and welded ignimbrite (Fig. 3). Welding refers to the processes of compaction and fusion of fragments that takes place at the time of deposition in sufficiently hot deposits (Broxton et al., 1995; Broxton and Reneau, 1995). High porosity portions of cooling units are typically nonwelded and are variably affected by vapor-phase crystallization. Nonwelded cooling units may be glassy or crystallized, depending on the degree of post-depositional devitrification of glass and/or vapor-phase crystallization in pores (Ross and Smith, 1961; Stimac et al., 1996). Glassy units typically have >60% wt. glass, and crystallized units have <10% wt. glass (Wilson, 2004).

The Otowi Member is a single cooling unit with a glassy nonwelded ignimbrite (Broxton et al., 1995; Gardner et al., 1999). The Tshirege Member mostly contains cooling units that are either welded ignimbrite or crystallized nonwelded ignimbrite (Broxton and Reneau, 1995; Wilson, 2004). Portions of Qbt1 and Qbt4, the lowermost and uppermost cooling units of the Tshirege Member, are glassy nonwelded ignimbrite, closely resembling the Otowi Member.

Welding zonation gives rise to predictable outcrop characteristics. Glassy, nonwelded ignimbrite weathers easily, producing broad debris aprons at the angle of repose and limiting outcrop. Welded ignimbrite forms cliffs. The welded ignimbrite outcrops are characterized by columnar cooling joints, which typically form pentagonal or hexagonal patterns on rare pavement surfaces (Fig. 4).

2.1. Mechanical stratigraphy of the Bandelier Tuff

For clarity and consistency with a basis in previous local work (Wilson et al., 2003, 2006), we apply two explicit definitions. The term 'fracture' in this study refers to discrete surfaces across which the rock has broken, lost cohesion, and has a measurable aperture. In contrast, deformation bands in the Bandelier Tuff are zones where reductions in clast size, pore size, and porosity accommodated cm-scale displacements. They are interpreted to be compactive shear deformation bands *sensu* Aydin et al. (2006), Fossen et al. (2007), and Schultz and Fossen (2008), but are hereafter referred to as 'deformation bands' for simplicity. Glassy nonwelded units contain deformation bands (Fig. 5a). Crystallized nonwelded units and an iron-oxidized portion of a glassy nonwelded unit have both deformation bands and fractures. Welded units exhibit only fractures (Fig. 5b).

Degree of welding and post-depositional crystallization also affects rock strength. Samples from the Bandelier Tuff exhibit increasing UCS with decreasing porosity (Fig. 6a; Day, 1993; Moon, 1993; Schultz and Li, 1995)), which correlates to increasing welding

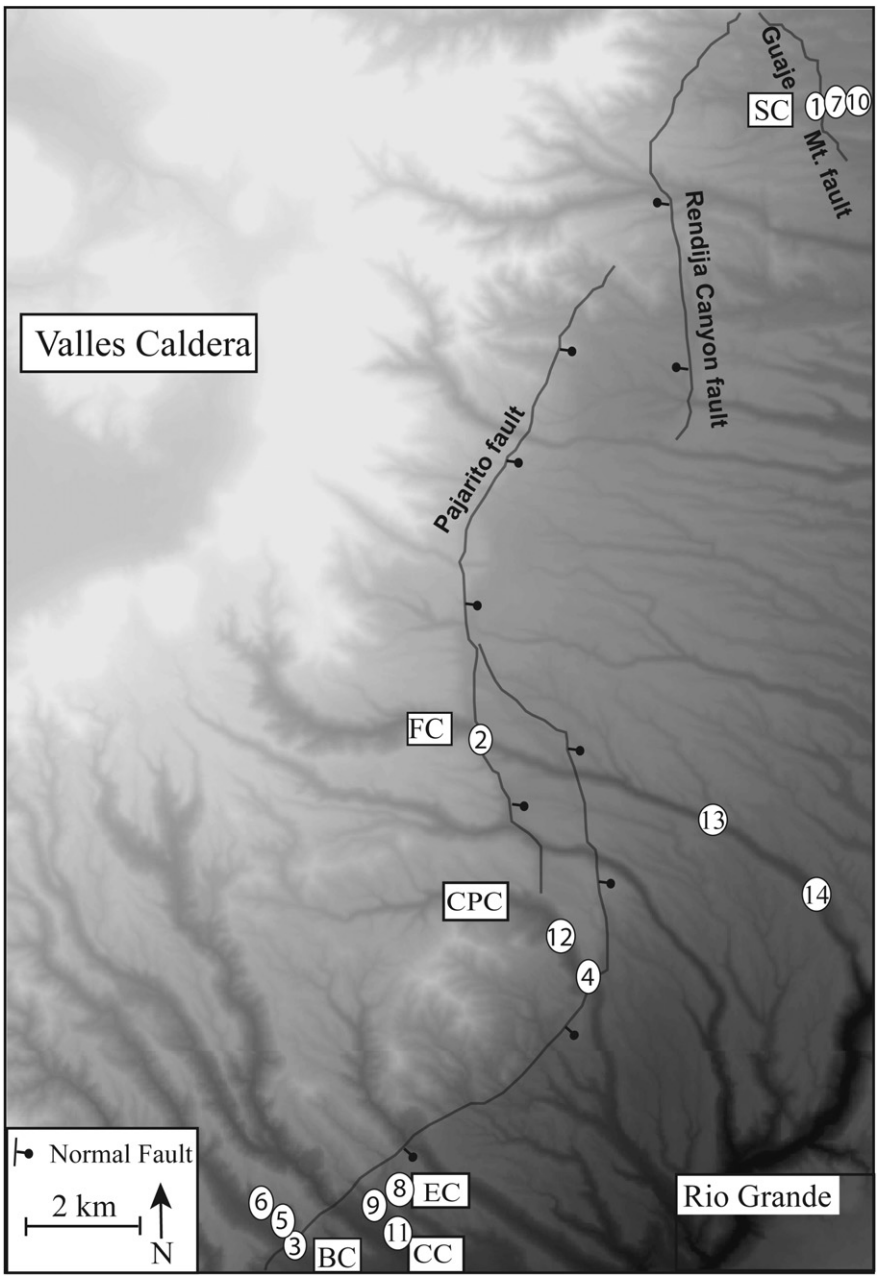

Fig. 2. Transect locations. Numbers correlate with Table 1, which provides detailed information about each transect. SC – Sawyer Canyon; FC – Frijoles Canyon; CPC – Capulin Canyon; EC – Eagle Canyon; CC – Cochiti Canyon; BC – Bland Canyon. Digital elevation model from Carey and Cole (2002). Location of map shown in Fig. 1.

and crystallization (Wilson et al., 2003). Consequently, the greatest UCS is likely exhibited by welded tuffs and the smallest associated with nonwelded tuffs (Fig. 6b; Quane and Russell, 2002).

3. Methods

To investigate the spatial distribution and orientation of fractures (including cooling joints) and deformation bands in nonwelded and welded ignimbrite of the Bandelier Tuff, observations were made along transects through E- to ESE-trending canyons, which cut across the Pajarito fault system (Table 1; Fig. 2). Because previous studies have shown that damage zone width varies with displacement (e.g., Shipton and Cowie, 2001; Fossen and Hesthammer, 2000; Shipton et al., 2006), we targeted study sites with different throw magnitude. Lewis et al. (2009) calculated throw from differences in surface elevation of the Tshirege Member across each map-scale fault in the Pajarito system, assuming minimal erosion subsequent to faulting. Throw on these map-scale faults exceeds 35 m, and is >100 m for all but three locations.

Transects were sited where exposure and access permitted. Cliff-forming welded unit exposures could not be safely accessed everywhere; nonwelded units are poorly exposed; and Los Alamos National Laboratory limits access for security reasons. We were able to study three transects through the welded unit that are essentially continuous for 290–390 m. In the poorly exposed glassy nonwelded units, however, transects are only 14 m to >100 m long, so we collected data from all 11 available sites, including 2 more than a kilometer from the fault zone. Along each transect, GPS coordinates and orientations of each structure were recorded (orientation data are in Supplementary Material). Structures were

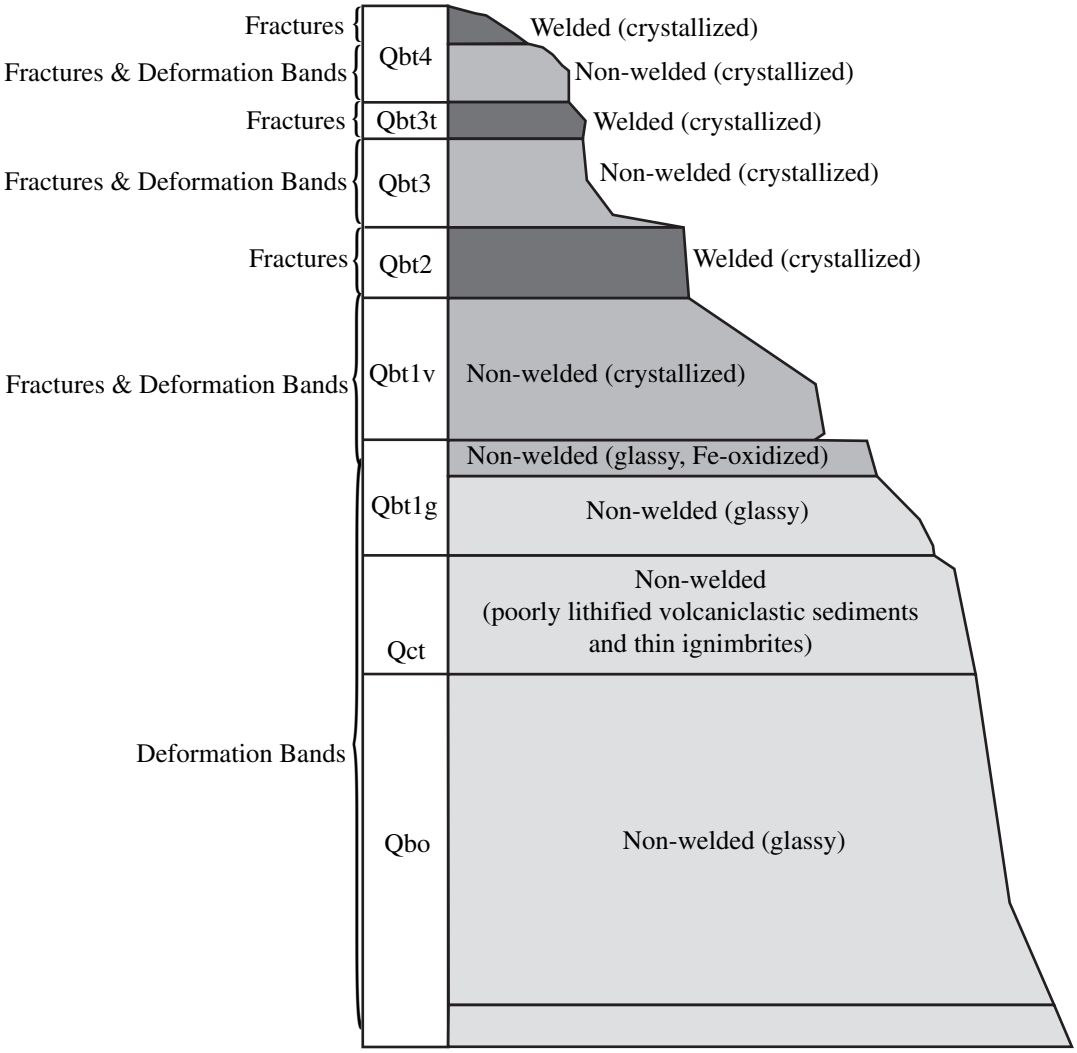

Fig. 3. Complete stratigraphic column showing relative thicknesses of the Bandelier Tuff cooling units. Cooling unit thicknesses vary with proximity to the caldera and paleotopography. Qbo – Otowi Member; Qct – Cerro Toledo interval; Qbt – Tshriege Member. Small-scale structures associated with each unit shown on left. Figure from Wilson (2004), modified after Broxton and Reneau (1995).

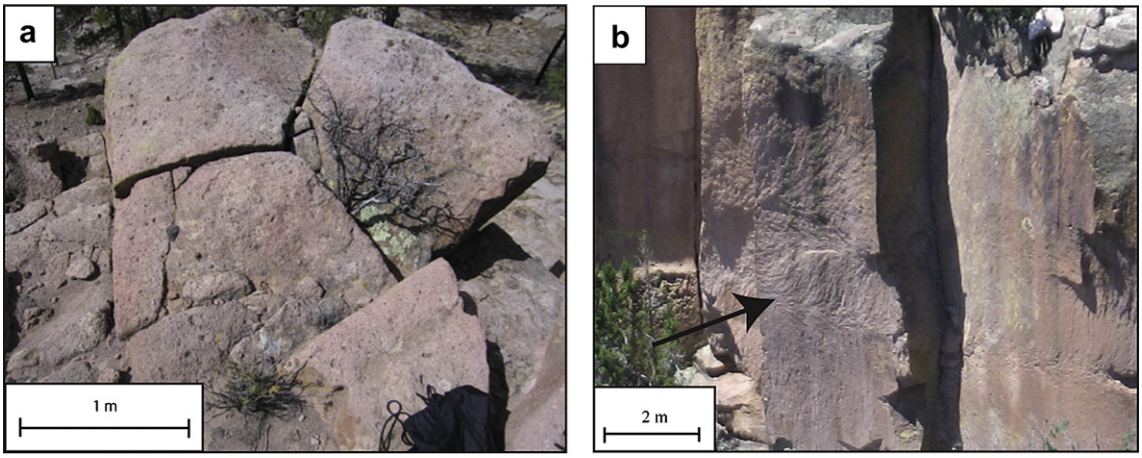

Fig. 4. a) Pavement showing columnar joint pattern. b) Typical character of walls of welded Qbt2 transects. Arrow points to plumose structure, which locally decorates cooling joint faces.

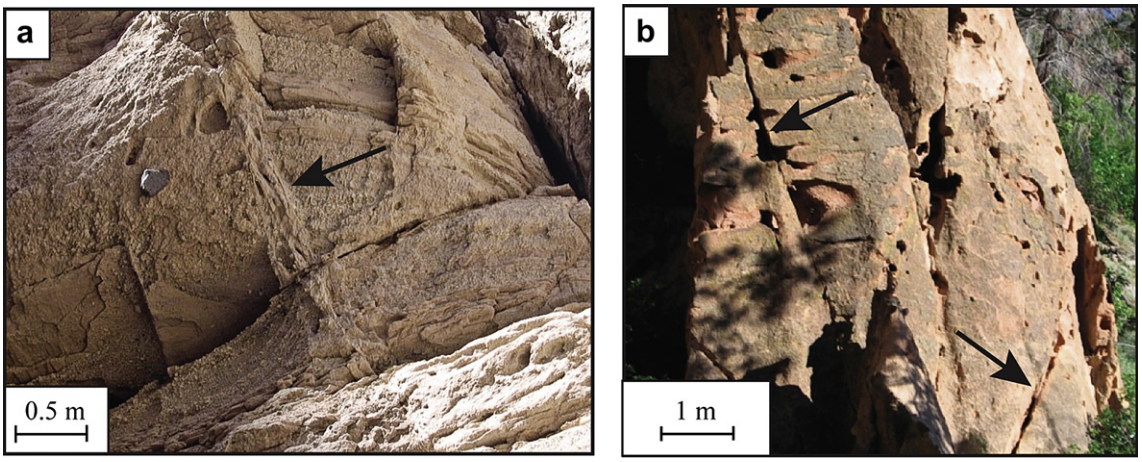

Fig. 5. Photographs of structures in Bandelier Tuff at Bandelier National Monument. a) Zone of anastomosing deformation bands (arrow) in glassy nonwelded Qbo, and b) discrete fractures (arrows) like these in crystallized nonwelded Qbt1v (refer to Fig. 2 for details of stratigraphy) are found in both crystallized no-welded and welded ignimbrites of the Bandelier Tuff.

plotted on a LIDAR image of the Pajarito fault system in ArcMap© to determine the distance to the nearest map-scale fault. Both orientations and densities of the structures are presented with respect to these distances.

Transect or scan-line sampling of linear features such as the traces of fractures introduces an orientation bias. Structures striking at smaller angles to the transect will be undersampled relative to those that are closer to perpendicular in strike to the transect (Terzaghi, 1965). A correction factor to minimize this orientation bias, where the number of observed features is divided by the sine of angle difference between trend and transect, has been developed (Terzaghi, 1965). However, when the angle equals 0°, a singularity is created, leading to the use of weighting factors instead (Terzaghi, 1965; Davy et al., 2006), sometimes as a function of the width of the sampling transect (borehole in these cases) versus the trace length of individual structures or the mean trace length for the structural population (Mauldon and Mauldon, 1997; Davy et al., 2006). A standard weighting factor has not been developed for outcrop data.

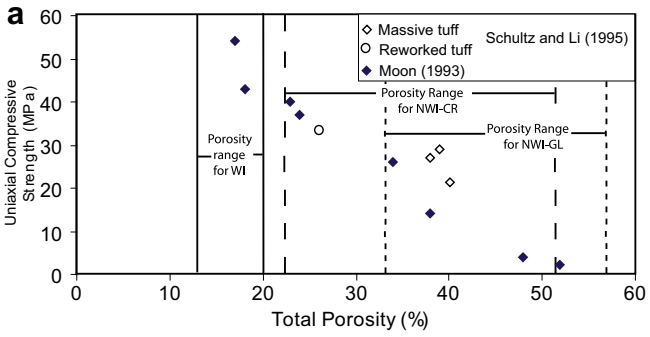

b

Rock Type	UCS range (MPa)	Mean UCS (MPa)
Bandelier Tuff (non-welded)	1.94-2.94	2.44
Chalk	2.3-4.0	3.1
Bandelier Tuff (partially welded)	9.65-15.91	12.78
Welded Tuff (Oregon)	20-23	22
Limestone (Indiana)	46-50	47
Berea Sandstone	72-76	74
Basalt (Cheakamus, B.C.)	132-164	148
Granite (Granite Is., B.C.)	177-187	181

Fig. 6. a) Unconfined compressive strength (UCS) of ignimbrites of varying porosity. Strength is inversely proportional to porosity. Porosity ranges from Wilson et al. (2003) are shown for comparison: WI = welded ignimbrite, NWI-CR = crystallized nonwelded ignimbrite, NWI-GL = glassy nonwelded ignimbrite. b) UCS of different rock types, including portions of the Bandelier Tuff (Quane and Russell, 2002).

Using cooling joints as a test population for sampling bias, we developed a weighting factor by comparing pavement with transect data. For each transect, ~20 cooling joint orientations were measured from ~16 m^2 pavement exposures (e.g., Fig. 4a) at locations shown in Fig. 7. These data are compared to data collected from sections of transects that show similar fracture densities both before and after bias correction (Fig. 8). Within the study area, polygons formed by cooling joints are generally pentagonal, but locally are hexagons (Fig. 4). In small pavements, where polygons are relatively uniform in size and shape, joint populations are trimodal (Fig. 8a–c). Previous transects through Bandelier Tuff sampled hundreds to thousands of joints, and typically report broad bimodal orientation populations rather than the discrete trimodal sets shown in Fig. 8a–c (see review by Lewis et al., 2009, and references therein). Our transect data also show bimodal populations, though with less spread in orientation than larger studies (Fig. 8d–f). We interpret the broad, bimodal patterns of joints measured over larger areas as being produced by spatial variations in the sizes and shapes of polygons.

The most even orientation distribution of joints is exhibited by pavement of Bland Canyon, which shows three essentially equally common joint sets, striking NW, E, and NE (Fig. 8b). The larger population measured in transect shows a broader distributions of poles to joints in WNW and NE-striking clusters (Fig. 8e). One cluster includes joints that strike at high angles to the transect line whereas the other has poles at low angles (<30°), including transect-parallel examples. We assume that each fracture set should be equally numerous, and those at a low angle have been undersampled. A weighting factor of two for fractures at <30° to the transect eliminates this inferred undersampling.

This correction factor was tested at the other two sites. Frijoles Canyon pavement has NNW-, E-, and NE-striking joints, but the E-striking joints are much less common (Fig. 8c). In this location, the larger population sampled in transect also exhibits two

Table 1
Transect descriptions, keyed by number to locations shown in Fig. 2.

Transect canyon	# on Fig. 6	Unit	Approximate transect orientation	Distance to main fault (m): (−) W of fault, (+) E of fault	HW or FW	Transect length (m)	Throw on nearest main fault
Sawyer Canyon	1	Qbt 2 (welded)	90°	−117 to +205	Both	332	35
Frijoles Canyon	2	Qbt 2 (welded)	120°	−141 to +244	Both	384	150
Bland Canyon	3	Qbt 2 (welded)	135°	−10 to +274	Both	290	90–100
Capulin Canyon	4	Qbo (nonwelded)	160°	+30 to +45	Graben	14	140
Bland Canyon	5	Qbo (nonwelded)	135°	−61 to −84	FW	19	90–100
Bland Canyon	6	Qbo (nonwelded)	135°	−148 to −183	FW	25	90–100
Sawyer Canyon	7	Qbt1g (nonwelded)	90°	+170 to +220	HW	65	35
Cochiti Canyon	9	Qbo (nonwelded)	135°	+230 to +310	HW	80	90–130
Eagle Canyon	8	Qbo (nonwelded)	135°	+315 to +390	HW	75	80–100
Sawyer Canyon	10	Qbt1g (nonwelded)	90°	+520 to +590	HW	46	35
Cochiti Canyon	11	Qbt1g (nonwelded)	135°	+635 to +710	HW	67	90–130
Capulin Canyon	12	Qbo (nonwelded)	160°	−715 to −790	FW	75	140
Frijoles Canyon	13	Qbt1g (nonwelded)	120°	+2450 to +2600	HW	175	150
Frijoles Canyon	14	Qbo (nonwelded)	135°	+3900 to +4100	HW	250	150

broader clusters of poles, which in this case are oblique to the transect. Application of the correction factor determined for Bland Canyon results in equal distributions of joints for Frijoles Canyon. At Sawyer Canyon, however, no correction factor would produce an even orientation distribution of poles to joints. As at Bland Canyon, Sawyer pavement has fewer E-striking joints than joints in other orientations. Transect data show two nearly overlapping populations of joints. These are roughly equally oblique to the transect line, and therefore equally likely to be sampled, but one population is smaller. We must conclude that in this location, cooling joints are more irregularly distributed. This example illustrates the limitations of our approach.

Our best constraints therefore lead us to impose a correction factor of two for fractures striking $<30^\circ$ to transects in welded ignimbrite. No reference state similar to cooling joints for the fractures is available to constrain a correction factor for deformation band orientations. For consistency, we use the same correction as applied to the fracture data.

4. Fractures and deformation bands in the Bandelier Tuff

4.1. Fracture density in welded unit Qbt2

Previous studies in Tshirege cooling unit Qbt2, the focus of this study, demonstrate cooling joint spacing of 6.6–10 per 10 m (Vaniman and Wohletz, 1990; Wohletz, 1995, 1996, Reneau and Vaniman, 1998). Fracture densities up to 17–23 per 10 m interval in the vicinity of faults have been interpreted as resulting from fault-zone deformation (Vaniman and Wohletz, 1990), but the width of damage zones around faults has not previously been measured. We evaluate whether this fracture density in rock units with cooling joints increases with proximity to faults (Fig. 7). Further, we define the domain of fault damage zones to be where fracture density is consistently $\geq$10 fractures/10 m, assuming that greater densities are due to the addition of fault-related fractures. This assumption is consistent with the qualitative observation that outcrops near faults exhibit more densely spaced fractures than protolith outcrops away from the faults (Fig. 9). Damage-zone fractures, however, rarely exhibit slickenlines or plumose structures, and cannot be simply characterized as shear and/or extensional fractures.

Two of the three transects (Sawyer, Frijoles) through the Qbt2 run from protolith, through fault damage zone, and end in the protolith, whereas one (Bland) runs from fault damage zone to hanging wall protolith (Figs. 2 and 7; Table 1). Considering corrected fracture densities, in the protolith average fracture densities are 7.1, 8.2, and 7.5 fractures/10 m for Sawyer, Bland and Frijoles Canyons, respectively (Fig. 7). Within the footwall damage zones, average fracture densities are 15.0, 37.0, 17.0 fractures/10 m for Sawyer, Bland and Frijoles Canyons, respectively. Within the hanging wall damage zones, fracture densities are 17.7, 20.6, and 17.7 fractures/10 m for Sawyer, Bland and Frijoles Canyons. Given that fault throw is greater from Sawyer to Frijoles Canyon, fracture densities in the damage zones do not correlate to throw magnitude.

Considering the overall width of the interpreted damage zones for each transect, they are 130 m or greater. The widths of footwall damage zones are 50 m, 10 m, and 50 m for Sawyer, Bland and Frijoles Canyons, respectively, although Bland Canyon consists of incomplete footwall data. The widths of hanging wall damage zones are 80 m, 160 m, and 160 m for Sawyer, Bland and Frijoles Canyons, respectively.

4.2. Welded unit fracture orientations

We report orientation data from transects through welded ignimbrite in a series of lower hemisphere equal-area net plots that compare uncorrected data with data that were contoured following application of the correction for orientation bias (Figs. 10–12). This correction weights poles to planes by stacking points, with one point added on top of the pole to each plane oriented $<30^\circ$ from the

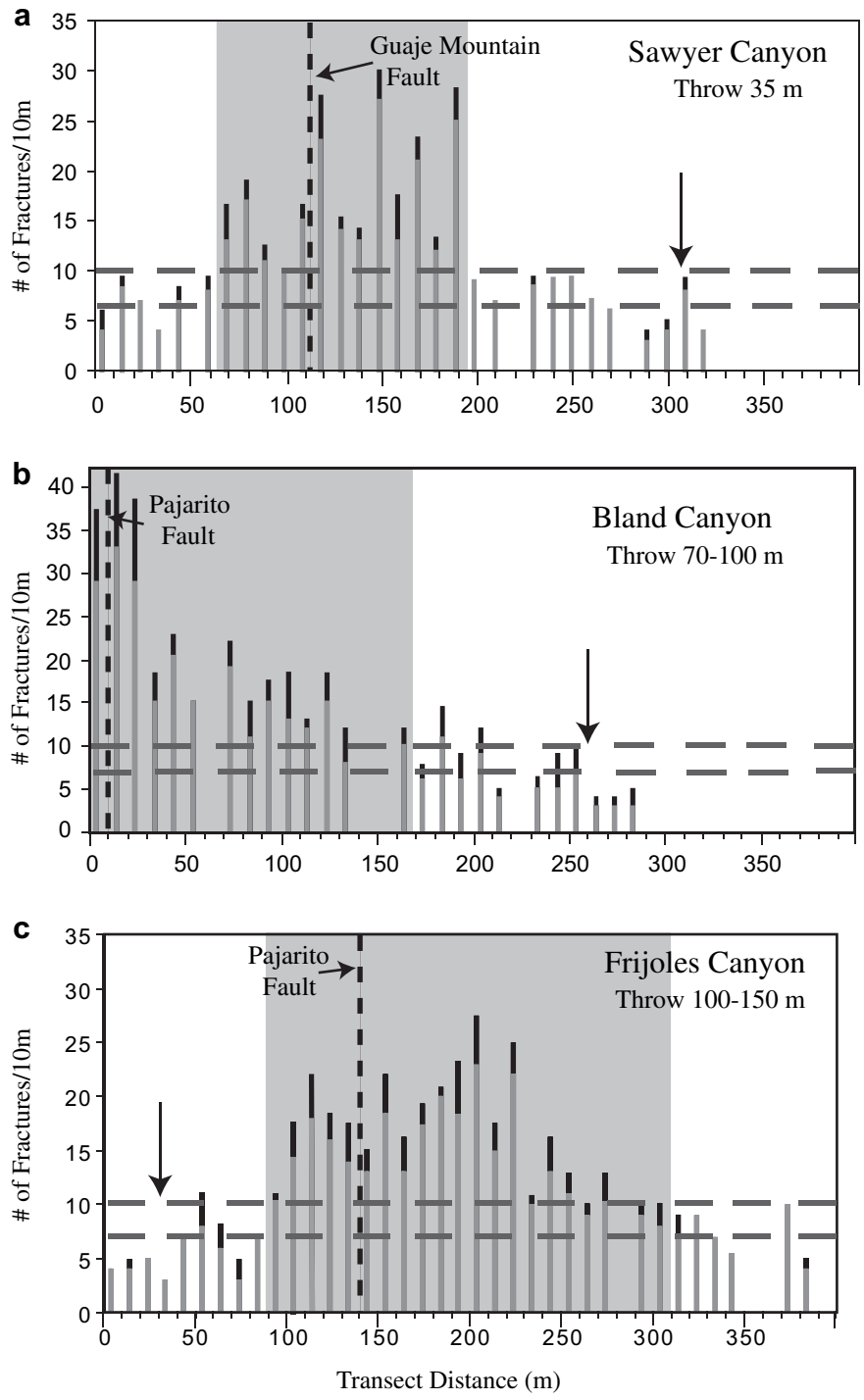

Fig. 7. Number of fractures per 10 m interval from transects in Qbt2 in a) Sawyer Canyon, b) Bland Canyon, and c) Frijoles Canyon (sites 1–3, Fig. 2 and Table 1). Fracture density shown as uncorrected (vertical gray bars) and corrected (vertical black bars) for scan-line bias. Transects ordered by magnitude of throw. Intervals with no data have no exposure. Shaded region encompasses the interpreted damage zone, where fracture density is consistently ≥10 fractures per 10 m. For each plot, the footwall is to the left (W), and the hanging wall is to the right (E). Arrows show location of pavements from which data shown in Fig. 8 were collected.

scan-line to achieve the weighting factor of 2. Thus, although the apparent distribution of poles does not change, contours of orientation data do change. Data are reported separately for footwall and hanging wall protolith and damage zones as defined in Fig. 7. Uncorrected data are provided for comparison.

Within the footwall damage zone in Sawyer Canyon, poles to fractures are more broadly distributed than in the other transects (Fig. 10). North-northeast-striking fractures dip steeply east and west; northwest-striking fractures dip steeply to the northeast and southwest. The hanging wall damage zone also exhibits north-northeast-striking fractures that dip steeply east and west and a smaller set of northwest-striking fractures, along with a few east-striking, near-vertical fractures. These damage zone fractures, though substantially more numerous, exhibit orientation

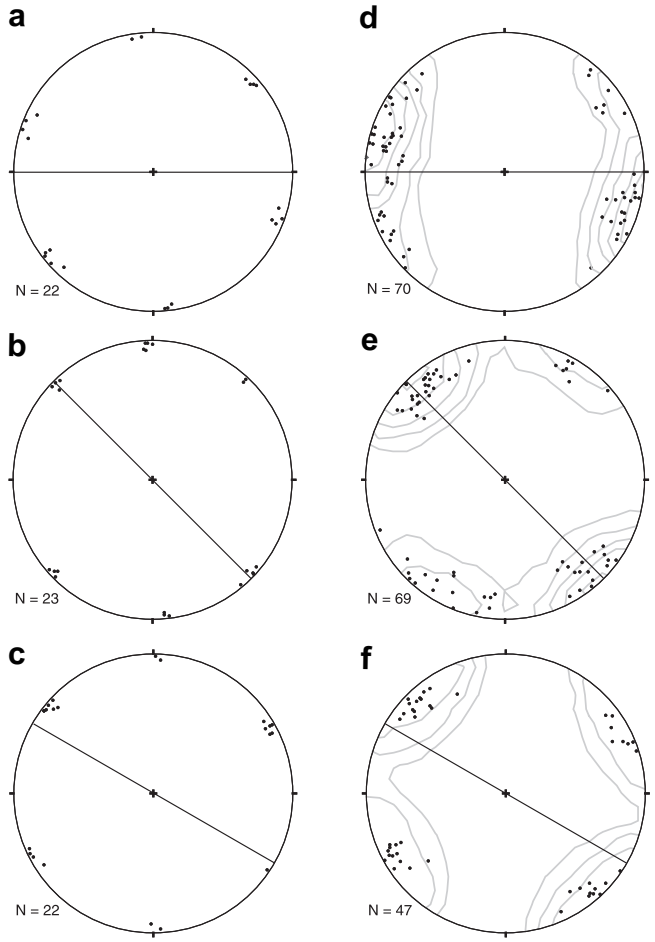

Fig. 8. a–c) Equal-area, lower-hemisphere plots of poles to cooling joints from pavement surfaces for (a) Sawyer, (b) Bland, (c) and Frijoles Canyons collected at locations shown in Fig. 7. d–f) Equal-area lower-hemisphere plots of poles to fracture planes collected along transects for (d) Sawyer, (e) Bland, and (f) Frijoles Canyons with Kamb (Kamb, 1959) contours (3σ contour interval), from the unshaded regions in Fig. 7 surrounding locations of pavement data collection. Solid lines indicate transect orientations.

distributions that are similar to adjacent protolith. The footwall damage zone exhibits a greater concentration of fractures that strike parallel to the Guaje Mt. fault, dipping both parallel and opposite to the fault, than the footwall protolith. Hanging wall damage zone fractures are more variable in both strike and dip than fractures in hanging wall protolith.

Bland and Frijoles canyon plots also show damage zone patterns similar to adjacent protolith (Figs. 11 and 12). In Frijoles Canyon, none of the fractures strike parallel to the Pajarito fault. Comparison of damage zone with adjacent protolith plots, however, suggests an increase in number of fractures parallel to the cooling joints that are closest in orientation to the fault in both corrected and uncorrected data. In Bland Canyon, corrected data show an increase in the numbers of fractures both sub-parallel and sub-perpendicular to the fault in the hanging wall damage zone. Hanging wall damage zone fractures, however, exhibit a wider range in dip than is shown by protolith cooling joints.

4.3. Deformation bands

Deformation bands in glassy nonwelded ignimbrite units Qbo and Qbt1g exhibit reduced grain size with respect to protolith. They are lighter in color where the surrounding protolith is orange, and darker where the protolith is gray. As noted earlier by Wilson et al. (2003, 2006), many deformation bands exhibit some evidence of preferential alteration and/or mineralization.

Due to the lack of primary structures such as bedding within individual cooling units, displacements typically could not be determined. In areas of high deformation band density, however, cross-cutting relationships between deformation bands and zones of deformation bands record normal throw. Zones of deformation bands with widths of 0.1–2 cm exhibit throw of 1–20 cm. True displacements may be higher if deformation bands accommodated a component of strike-slip motion.

The extent to which deformation bands cross cooling units is difficult to establish. In most cases, deformation bands can be traced for >15 m parallel to dip, but the ends are either too high for observation or covered by debris and vegetation. The exceptions are deformation bands that end abruptly at the contact between the fine-grained Qbo and the conglomeratic Qct.

4.4. Deformation band density

The eleven sites studied in glassy nonwelded Qbo and Qbt1g range from 30 to 45 m to ~4000 m from map-scale faults (Fig. 2, Table 1). Poor exposure of glassy nonwelded units forces grouping of footwall with hanging wall data in a plot of deformation band density with distance from nearest map-scale fault, which has been corrected for scan-line bias (Fig. 13). These data illustrate that more than 310 m from map-scale faults, deformation band density is consistently less than 3.0 per 10 m. Between 310 and 148 m, deformation band density increases slightly to 4.0 per 10 m. Closer to the fault zone, however, deformation band density increases exponentially with 17.8 deformation bands per 10 m at 61–84 m increasing to 92.0 per 10 m at 30–45 m from a map-scale fault. The 30–45 m transect is located in a horst between the Pajarito fault and a subsidiary fault (120 m and 8 m of throw, respectively), which also may influence deformation band density.

4.5. Deformation band orientations

Orientation data were grouped on the basis of similarity, with data from each transect rotated with respect to the strike of the nearest major fault, shown as north-striking and steeply E-dipping in Fig. 14, to facilitate comparison between data collected from traverses in different parts of the fault system. Thus, the data are presented in a fault reference frame rather than a geographic reference frame. For the transect located in a horst between the Pajarito fault and a smaller, west-side-down fault, the physically closer, smaller fault orientation is also shown (dashed lines in Fig. 14a). All orientation data has been corrected for scan-line bias.

Deformation bands within 84 m of map-scale faults are well organized (Fig. 14a). Most dip to the east, but a significant subset with similar strike dip to the west. Collectively, these deformation bands are distinctly oblique to the main fault. They are closer in orientation, but largely oblique to, the subsidiary fault forming the horst in Capulin Canyon.

With increasing distance from the fault system, deformation bands exhibit a wider range of orientations. Between 148 and 220 m, deformation bands exhibit no preferred orientation (Fig. 14b). Farther from the fault, they are locally oriented at a high angle to the Pajarito fault system (Fig. 14c), but in places exhibit an obliquity similar to that nearer mapped faults (compare Fig. 14a and c). These data sets are small due to low deformation band density, but cumulatively show less organization than transects nearer the fault system.

Most of the data obtained from glassy nonwelded ignimbrite come from the hanging wall. If a boundary to the hanging wall

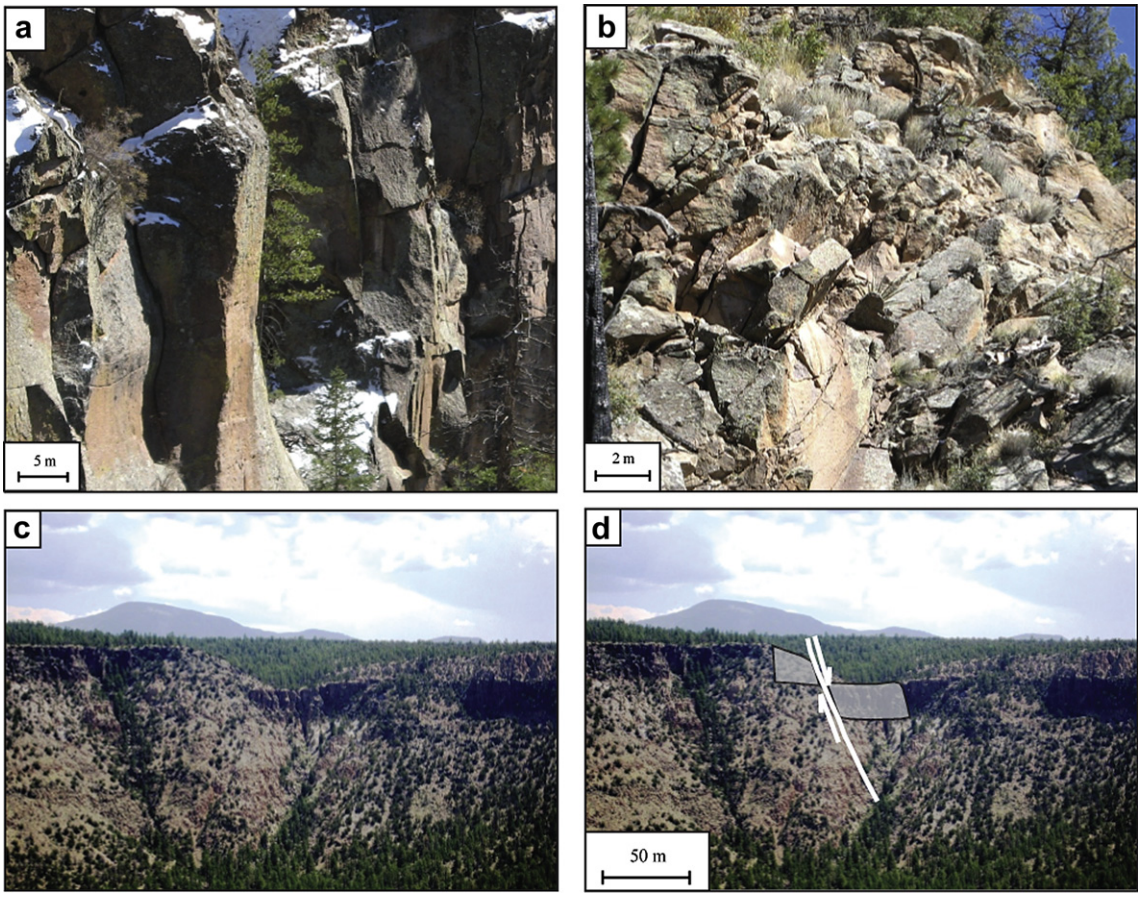

Fig. 9. Within welded units, fractures are relatively widely spaced outside the damage zone (a), but are closely spaced within the damage zone (b) resulting in broken apart rock. c) Photograph of fault cutting Qbt2. Damage zone (gray) and fault (white) outlined in (d).

damage zone is drawn as in welded unit Qbt2, based on elevation of structure density above background, it would be ~300 m from the fault (Fig. 13). On the basis of deformation band orientations, a better choice would be between 84 and 148 m from the fault system, where deformation bands begin to exhibit a higher level of organization (Fig. 14a, b). This also represents the location of an exponential increase in deformation band density (Fig. 13). An estimate of 100 m footwall damage zone width (between 84 and 148 m from the fault) is conservative, but nonetheless is double the footwall damage zone width documented in welded unit Qbt2.

5. Discussion

Damage zone width has been shown to increase with displacement, but the magnitude of increase in width with displacement varies from fault to fault (Shipton et al., 2006 and references therein). These different relationships have been attributed to variations in dominant deformation mechanisms (e.g., fracture versus deformation band) in different lithologies, changes in rheology over time, and differences in deformation conditions (Shipton et al., 2006). Variations in width at a given displacement could also be attributed to these controlling variables. Deformation conditions in the different young, near-surface deposits of the Bandelier Tuff were essentially identical. Thus, differences in extrinsic variables such as confining pressure or strain rate cannot explain the variation in damage zone width. In the following sections, we explore other potential controls on damage zone width.

5.1. Primary lithologic controls on damage-zone structure and width

Both this and previous studies have noted that degree of welding influences the dominant deformation mechanisms in different ignimbrites (Wilson et al., 2003; Evans and Bradbury, 2004; Wilson, 2004). On the volcanic island of Gran Canaria, near-surface normal faulting of highly to moderately welded ignimbrite results in a damage zone of closely spaced fractures, whereas poorly welded units fail through the formation of deformation bands (Shipton et al., 2006). On Gran Canaria, damage-zone joint density is inversely proportional to unit thickness and increases with proximity to the fault core. In the Pajarito fault zone, joint density is more variable, which we attribute to the influence of pre-existing cooling joints. Here we consider first what controls the types of structures that form in ignimbrites with different petrophysical properties and second, whether these same factors or the different structures themselves affect damage zone width.

Previous workers have identified porosity as the fundamental petrophysical property influencing the types of structures that form in damage zones (e.g., Dunn et al., 1973; Wong et al., 1997; Wong and Zhu, 1999; Schultz and Siddharthan, 2005). Sandstones with porosity >10% typically exhibit deformation band damage zones, where porosity, grain size, and permeability are reduced by shear in 1-2 mm wide deformation bands (e.g., Antonellini and Aydin, 1994; Sigda et al., 1999). All ignimbrites studied on the Pajarito Plateau, however, have porosity >10% as even the welded ignimbrites have

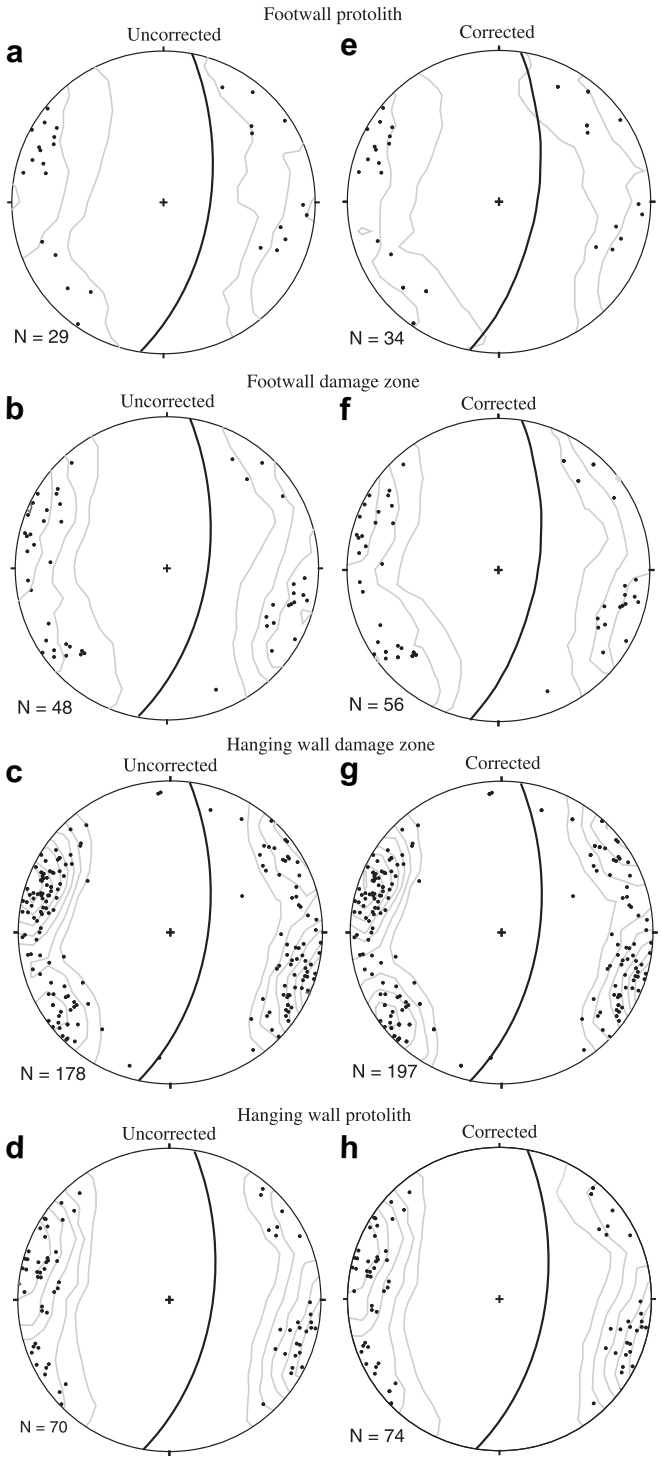

Fig. 10. Fracture orientation data from Sawyer Canyon. a–d) Uncorrected plots of poles to fracture planes. e–h) Corrected plots of poles to fracture planes. Plot contouring parameters as given in Fig. 8. Local trace of the Guaje Mt. fault (great circle) shown for reference.

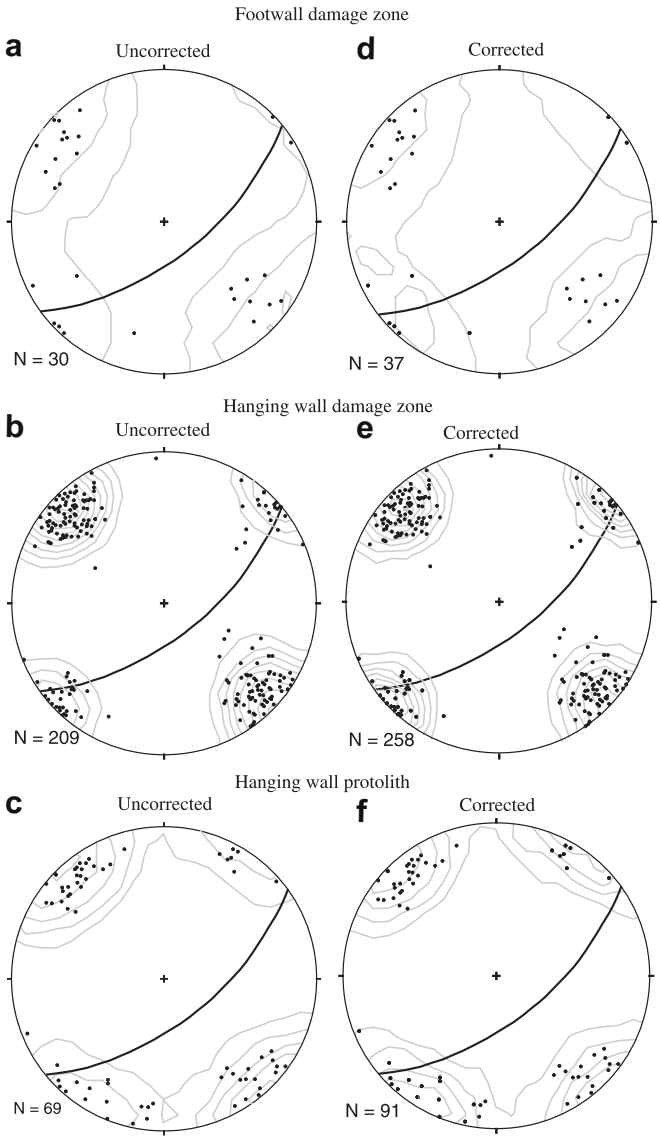

Fig. 11. Fracture orientation data from Bland Canyon. a–c) Uncorrected plots of poles to fracture planes. d–f) Corrected plots of poles to fracture planes. Plot contouring parameters as given in Fig. 8. Plot also shows the local trace of the Pajarito fault (great circle).

porosities between ~13 and 20% (Wilson et al., 2003; Fig. 6). This observation suggests that porosity is a necessary but not sufficient condition for the formation of deformation bands. Welding involves both compaction, which increases clast contact area, and fusion of clast margins, resulting in a substantial increase in grain contact strength. In addition, welded units exhibit devitrification and vapor-phase crystallization, processes that occur during cooling of the units and that reduce glass content in the Bandelier Tuff from >60% to <10% (Wilson, 2004; Wilson et al., 2006). We propose that these processes substantially strengthen both grain contacts and the solid framework of a tuff, allowing it to support throughgoing fractures without the development of deformation bands.

This analysis begs the question of whether these petrophysical properties control damage-zone width as well as type of damage zone structure. Previous workers have shown that damage zone width varies with the strength of the faulted geomaterial. For example, a clay content of ≥10% can reduce fault-zone width in sandstone by ~75% (Antonellini and Aydin, 1995). Similarly, a significant proportion of clay beds in heterolithic sequences can reduce fault-zone width to an even greater extent (Heynekamp et al., 1999). In the Bandelier Tuff, however, weaker nonwelded glassy ignimbrite has a wider footwall damage zone than stronger welded ignimbrite, suggesting a different relationship than observed with interbedded clays.

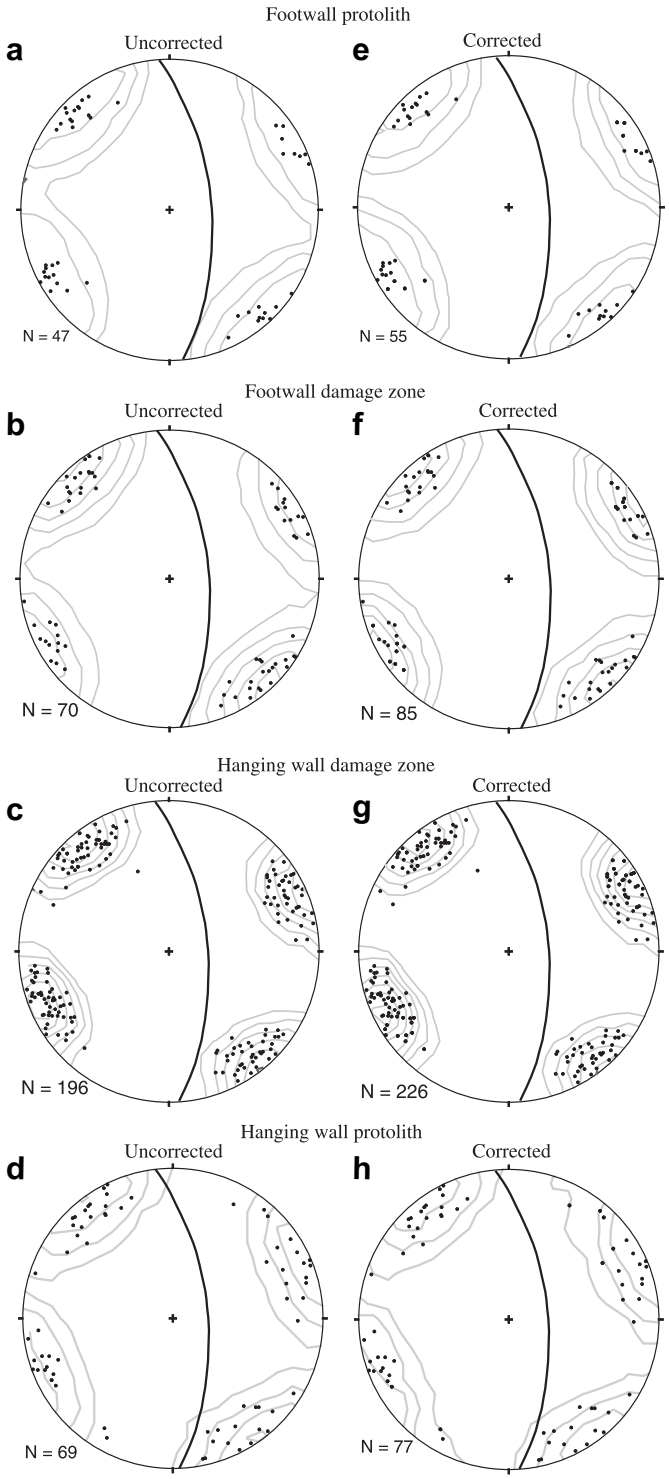

Fig. 12. Fracture orientation data from Frijoles Canyon. a–d) Uncorrected plots of poles to fracture planes. e–h) Corrected plots of poles to fracture planes. Plot contouring parameters as given in Fig. 8. Local trace of the Pajarito fault (great circle) shown for reference.

Fossen and Hesthammer (2000) and Shipton and Cowie (2001) argued that deformation bands are mechanically distinct from discrete slip surfaces or shear fractures, and fault zone scaling relationships should reflect that distinction. Since deformation bands are stronger than protolith (due to pore collapse and grain-size reduction) and fractures are weaker (due to loss of cohesion), deformation should be more localized in a fracture-based damage zone. In the Bandelier Tuff, however, the preferential alteration and mineralization of deformation bands in some locations is interpreted to be sufficient to localize strain, with evidence of multiply reactivated clay-rich deformation bands, as well as slip surfaces forming on calcite–cemented deformation bands (Wilson et al., 2006). Furthermore, even directly adjacent to faults, deformation bands rarely form the dense, wide clusters and slip surfaces described in sandstone (e.g., Aydin and Johnson, 1978; Antonellini and Aydin, 1994; Myers and Aydin, 2004), suggesting that widening of damage zones associated with strengthening due to deformation band formation is not a viable hypothesis.

The structures present in the Pajarito fault damage zones are not all tectonic. Cooling joints with apertures ranging from 3.0 to 12.5 mm are pervasive in welded unit Qbt2 (Vaniman and Wohletz, 1990; Wohletz, 1995, 1996; Reneau and Vaniman, 1998). We infer these have a m-scale weakening effect that is not evaluated in the core-scale unconfined compressive strength experiments documented in Fig. 6. Although fracture density demonstrably increases in damage zones (Fig. 7), significant fault-zone strain could be taken up by dilation, contraction, and/or shear on existing cooling joints (Lewis et al., 2009). This hypothesis is consistent with our interpretation that the footwall fracture damage zones are half the size of the footwall deformation-band damage zones (Figs. 7 and 13).

For welded unit Qbt2, we found the hanging wall damage zone to be wider than the footwall damage zone, an observation demonstrated in other locations to be the result of variations in lithology or local folding (e.g., Heynekamp et al., 1999; Berg and Skar, 2005). Given that our observations are from a single lithology and that no other secondary structures such as folds or small map-scale faults are present along our transects (Lewis et al., 2009), this asymmetry must have other causes. Two possible explanations are offered for the observed asymmetry, both of which require additional research to validate. The two hypotheses are based on the observation that the width of the hanging wall damage zone increases with displacement, but the width of the footwall damage zone apparently reaches a maximum of ~50 m and then ceases to grow wider. First, after Qbt2 in the footwall was exhumed by down-dip movement of the hanging wall, it ceased to accumulate displacement-related deformation. Second, the near-surface location of the Bandelier Tuff rocks in the hanging wall puts them in the dilational quadrant for normal fault motion, resulting in preferential hanging wall extension with slip (Zhang and Sanderson, 1996).

5.2. Variations in orientation of structures with lithology and location

Glassy nonwelded ignimbrites lack both welding, which produces a sub-horizontal foliation, and cooling joints, which produce sub-vertical columns of different shapes. Therefore, we interpret nonwelded ignimbrite to be materially isotropic. Because of this absence of primary anisotropy, we expect the orientation modes of deformation bands to reflect only fault-zone deformation. Deformation bands, however, largely strike oblique to the Pajarito fault system, which is not consistent with simple normal faulting.

Previous workers have suggested that many of the north- to north-northeast-striking faults of the Rio Grande rift are older structures, reactivated as the region extended (Beck and Chapin, 1994; Karlstrom et al., 1999; Behr et al., 2004; Sanders et al., 2006). Others provided evidence that the rift records left-lateral oblique opening, rather than pure normal extension (Kelley, 1982;

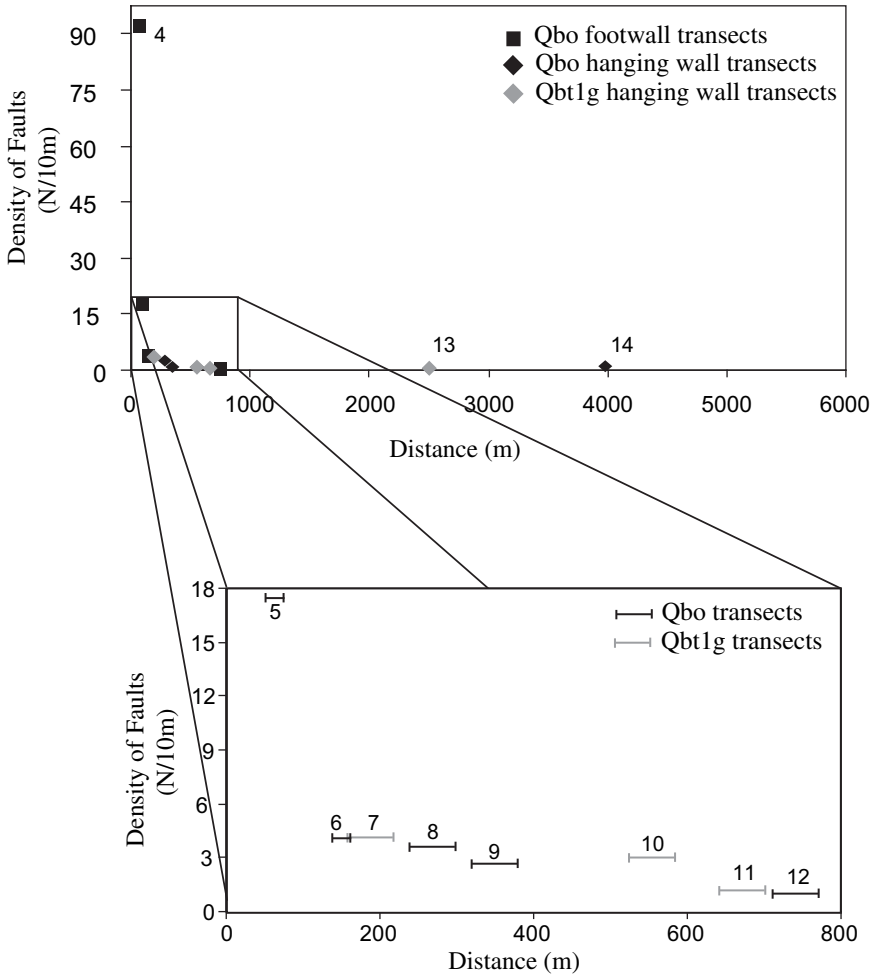

Fig. 13. In glassy nonwelded Qbo and Qbt1g deformation band density is high adjacent to the major faults, but drops abruptly within ~100 m. At ~300 m, deformation band density falls below 0.5 per 10 m, and is essentially constant to 4.1 km from major faults. Brackets indicate transect length. Numbers next to brackets correspond to the numbered transects in Fig. 2 and Table 1.

Chapin and Cather, 2004; Salyards et al., 1994; Lewis and Baldridge, 1994). Structures documented in trenches across segments of the Pajarito fault system have been interpreted as recording left-lateral oblique slip (Lewis et al., 2009). The majority of the deformation bands that we measured in the fault damage zone strike counter-clockwise to the Pajarito fault. Where slip sense can be determined, they record normal motion. This obliquity and slip sense of shear deformation bands is consistent with left-lateral oblique normal slip on the Pajarito fault and with the regional tectonic data.

The orientations of fractures within damage zones in welded ignimbrite of the Bandelier Tuff vary along strike, but in every case are similar to the dominant orientations of cooling joints in adjacent protolith (Figs. 8, 10–12). The primary difference is that damage zones have a greater percentage of fractures that dip more moderately, whereas fractures in the protolith mainly dip >80°. Fracture density is much greater in the damage zones than in the protolith, with more than 30 fractures per 10-m interval locally in the fault zone versus a maximum of 10 fractures per 10-m interval outside. If we compare numbers of fractures in different orientations, fault-zone fractures form most commonly sub-parallel to the strike of the cooling joints that are most similar in strike to the nearest major fault, but with a greater range of dip magnitudes (Figs. 8, 10–12).

Pre-existing mechanical anisotropy can influence the formation of new fractures (e.g., Peacock and Sanderson, 1992). We propose that the formation of fractures sub-parallel to cooling joints reflects joint-produced mechanical anisotropy and heterogeneity. The formation of a fracture reduces the stress in its immediate vicinity (e.g., Pollard and Segall, 1987) and creates a local stress state different from the remote stress, influencing future fracture formation and propagation (Lachenbruch, 1962; Pollard et al., 1982; Segall and Pollard, 1983; Segall, 1984; Olson and Pollard, 1989; Olson, 1993). We infer that the local rotation of principal stresses to positions parallel and perpendicular to the free surfaces produced by cooling joints resulted in the formation of new fractures sub-parallel to the joints. The observation of new joints approaching normal to, but then aligning parallel to older columnar joints in lava flows (Pollard and Aydin, 1988) supports this assertion. Given that the newly formed fractures in the welded unit damage zones generally lack evidence for either shear (e.g., slickenlines, offset markers) or extension (e.g., plumose structures), the nature of the stress perturbation cannot be specifically characterized. Still, we believe this interpretation is appropriate, since we observe newly formed damage zone fractures subparallel to cooling joints, rather than in orientations synthetic and antithetic to the nearest map-scale fault.

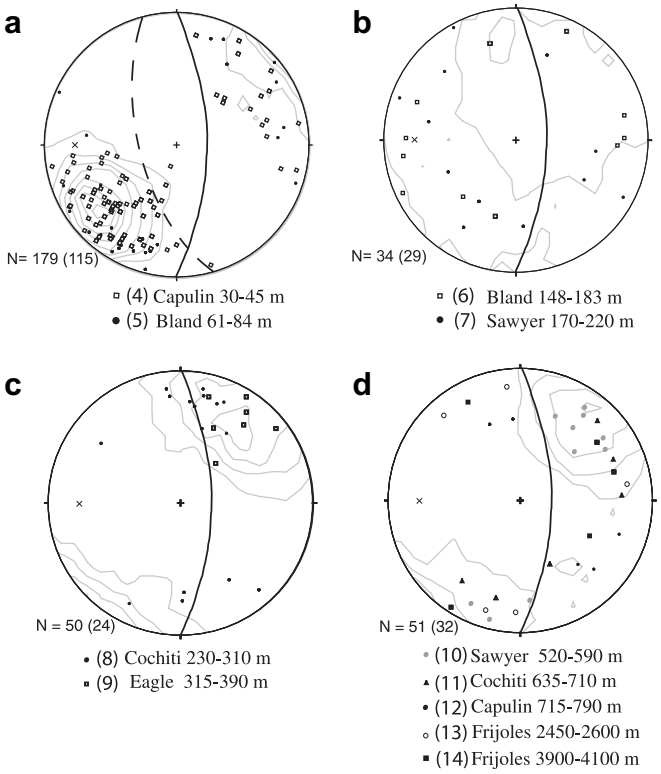

Fig. 14. Kamb-contoured (3σ contour interval) equal area, lower hemisphere plots of corrected poles to deformation bands in glassy nonwelded units of the Bandelier Tuff. Data for each transect have been rotated as described in the text, so that all deformation band orientations are shown with respect to the adjacent map-scale fault orientation (solid great circles, pole to plane indicated by x). Data are plotted for traverses with increasing distance from map-scale faults from a) to d). Symbols indicate data from specific traverses, as shown in keys. Dashed great circle in a) is trace of local 8 m displacement fault in Capulin Canyon. Numbers next to transect names are keyed to Table 1 and Fig. 2. N = corrected number of fractures (uncorrected number in parentheses).

6. Conclusions

The structural character and width of the Pajarito fault zone vary across different cooling units of the Bandelier Tuff. Welded ignimbrite produces fracture damage zones, whereas nonwelded ignimbrite damage zones consist of deformation bands (Wilson et al., 2003). Because all of these rocks have porosities >13%, this difference is attributed to the strengthening effect of welding and post-depositional crystallization. This strengthening does not, however, explain the fact that footwall damage zone width is smaller in welded than in glassy nonwelded units. We attribute this difference to the m-scale weakening effect of pre-existing cooling joints, which localizes strain in welded units.

Fracture damage zones developed in welded ignimbrite show an asymmetry distinct from that of glassy nonwelded ignimbrite. Fractures in the damage zones are, at each location studied, subparallel to cooling joints in the protolith. We interpret the formation of new fractures parallel to pre-existing cooling joints to be fundamentally controlled by inherited mechanical anisotropy. Because cooling joints vary spatially in orientation, damage zone asymmetry also varies along strike of the fault system.. Where the faulted rock is mesoscopically isotropic, however, in glassy nonwelded ignimbrite, the orientation distribution of deformation bands is also asymmetric. Damage zone deformation bands are highly organized in conjugate sets oblique to map-scale faults. The obliquity is consistent with oblique left-lateral normal extension across the Pajarito fault system, suggesting that, like other faults in the Rio Grande rift, the Pajarito system may reactivate an older structure.

Collectively, these observations indicate that the fault zones that constitute the Pajarito system are not deforming by plane strain. In this case, the departure from plane strain reflects the influence of inherited structures at both the regional and local scales. The resulting asymmetry is difficult to predict, but should be suspected wherever pre-existing anisotropy has been documented.

The observations of damage zone width and character in this study have implications for future work on modeling fluid flow through fault zones. In a single fault zone, damage zone width, hydrologically significant structures, and anisotropy of permeability can all vary with lithology. These points should be considered in collecting data to construct and parameterize models investigating the influence of faults on fluid flow and contaminant transport.

Acknowledgements

This research was supported by IGPP grants 1121R and 10594-001-05. PR thanks T. Johnson and C. Schuettpelz for support/guidance in the field. We thank S. Ralser for assistance with photographs. Detailed constructive reviews by D. Sanderson and C. Okubo significantly improved the manuscript.

Appendix. Supplementary material

Supplementary data associated with this article can be found in the online version at doi:10.1016/j.jsg.2010.05.005.

References

Antonellini, M.A., Aydin, A., 1994. Effect of faulting on fluid flow in porous sandstones: petrophysical properties. American Association of the Petroleum Geologists Bulletin 78, 355–377.
Antonellini, M., Aydin, A., 1995. Effect of faulting on fluid flow in porous sandstones; geometry and spatial distribution. AAPG Bulletin 79, 642–671.
Aydin, A., Johnson, A.M., 1978. Development of faults as zones of deformation bands and as slip surfaces in sandstone. Pure and Applied Geophysics 116, 931–942.
Aydin, A., Borja, I.R., Eichhubl, P., 2006. Geological and mathematical framework for failure modes in granular rocks. Journal of Structural Geology 28, 83–98.
Baldridge, W.S., Keller, G.R., Haak, V., Wendlandt, E., Jiracek, G.R., Olsen, K.H., 1995. The Rio Grande rift. In: Olsen, K.H. (Ed.), Continental Rifts: Evolution, Structure, Tectonics, pp. 233–275.
Beck, W.C., Chapin, C.E., 1994. Structural and tectonic evolution of the Joyita Hills, central New Mexico; implications of basement control on Rio Grande Rift. In: Keller, G.R., Cather, S.M. (Eds.), Basins of the Rio Grande Rift; Structure, Stratigraphy, and Tectonic Setting. Geological Society of America Special Paper, vol. 291, pp. 187–205.
Behr, R., Goodwin, L.B., Kelley, S.A., 2004. Structural and thermochronological constraints on the movement history of the Montosa Fault, New Mexico. New Mexico Bureau of Geology & Mineral Resources Bulletin Report 160, 139–160.
Berg, S.S., Skar, T., 2005. Controls on damage zone asymmetry of a normal fault zone: outcrop analyses of a segment of the Moab fault, SE Utah. Journal of Structural Geology 27, 1803–1822.
Broxton, D., Heiken, G., Chipera, S.J., Byers, F.M., 1995. Statigraphy, petrography, and mineralogy of Bandelier Tuff and Cerro Toledo deposits, in Earth Science Investigations for Environmental Restoration—Los Alamos National Laboratory Technical Area 21. In: Broxton, D.E., Eller, P.G., (Eds.), Los Alamos National Laboratory Report LA-12934-MS, pp. 33–64.
Broxton, D., Reneau, S., 1995. Stratigraphic nomenclature of the Bandelier Tuff for the Environmental Restoration Project at Los Alamos National Laboratory. Los Alamos National Laboratory Report LA-13010-MS.
Broxton, D., Vaniman, D., 2005. Geologic framework of a groundwater system on the margin of a rift basin, Pajarito Plateau, north-central New Mexico. Vadose Zone Journal 4, 522–550.
Caine, J.S., Evans, J.P., Forster, C.B., 1996. Fault zone architecture and permeability structure. Geology 24, 1025–1028.
Carey, W.J., Cole, G., 2002. Description of the Cerro Grande fire laser altimetry (LIDAR) data set. Los Alamos National Laboratory Report LA-13892-MS.
Carter, K.E., Winter, C.L., 1995. Fractal nature and scaling of normal faults in the Española Basin, Rio Grande rift, New Mexico: implications for fault growth and brittle strain. Journal of Structural Geology 17, 863–873.

Chapin, C.E., Cather, S.M., 2004. Tectonic setting of the axial basins of the northern and central Rio Grande Rift. In: Keller, G.R., Cather, S.M. (Eds.), Basins of the Rio Grande Rifts; Structure, Stratigraphy, and Tectonic Setting. Geological Society of America Special Paper, 291, pp. 5–25.
Chester, F.M., Evans, J.P., Biegel, R.L., 1993. Internal structure and weakening mechanisms of the San Andreas faults. Journal of Geophysical Research 98, 771–786.
Davy, P., Darcel, C., Bour, O., Munier, R., de Dreuzy, J.R., 2006. A note on the angular correction applied to fracture intensity profiles along drill core. Journal of Geophysical Research 111, B11408. doi:10.1029/2005JB004121.
Day, R.W., 1993. Engineering properties of nonwelded tuff. Bulletin of the Association of Engineering Geologist 30, 121–126.
Dunn, D.E., LaFountain, L.J., Jackson, R.E., 1973. Porosity dependence and mechanism of brittle fracture in sandstones. Journal of Geophysical Research 78, 2403–2417.
Evans, J.P., Bradbury, K.K., 2004. Faulting and fracturing of nonwelded Bishop Tuff, Eastern California: deformation mechanisms in very porous materials in the vadose zone. Vadose Zone Journal 3, 602–623.
Faulkner, D.R., Mitchell, T.M., Healy, D., Heap, M.J., 2006. Slip on 'weak' faults by the rotation of regional stress in the fracture damage zone. Nature 444, 922–925.
Faulkner, D.R., Mitchell, T.M., Rutter, E.H., Cembrano, J., 2008. On the structure and mechanical properties of large strike-slip faults. In: Wibberly, C.A.J., Kurz, W., Imber, J., Holdsworth, R.E., Collettini, C. (Eds.), The Internal Structure of Fault Zones: Implications for Mechanical and Fluid-flow Properties. Geological Society of London Special Publication, vol. 299, pp. 139–150.
Fossen, H., Hesthammer, J., 2000. Possible absence of small faults in the Gullfaks Field, northern North Sea; implications for downscaling of faults in some porous sandstones. Journal of Structural Geology 22, 851–863.
Fossen, H., Schultz, R.A., Shipton, Z.K., Mair, K., 2007. Deformation bands in sandstone: a review. Journal of the Geological Society 164, 755–769.
Gardner, J.N., Goff, F., 1984. Potassium-argon dates from the Jemez volcanic field: implications for tectonic activity in the north-central Rio Grande rift. New Mexico Geological Society Guidebook 35, 75–81.
Gardner, J.N., Lavine, A., WoldeGabriel, G., Krier, D., Vaniman, D., Caporuscio, F., Lewis, C., Reneau, P., Kluk, E., Snow, M.J., 1999. Structural geology of the northwestern portion of Los Alamos National Laboratory, Rio Grande Rift, New Mexico: implications for seismic surface rupture potential from TA-3 to TA-55. Los Alamos National Laboratory Report LA-13589-MS.
Gardner, J.N., Reneau, S.L., Lewis, C.J., Lavine, A., Krier, D.J., WoldeGabriel, G., Duthrie, G.D., 2001. Geology of the Pajarito Fault Zone in the Vicinity of S-Site (TA-16). Los Alamos National Laboratory, Rio Grande Rift, New Mexico. Los Alamos National Laboratory Report LA-13831-MS.
Haneberg, W.C., 1995. Steady state groundwater flow across idealized faults. Water Resources Research 31, 1815–1820.
Heynekamp, M.R., Goodwin, L.B., Mozley, P.S., Haneberg, W.C., 1999. Controls on fault-zone architecture in poorly lithified sediments, Rio Grande Rift, New Mexico: implications for fault-zone permeability and fluid flow. In: Haneberg, W., Mozley, P., Moore, J., Goodwin, L. (Eds.), Faults and Subsurface Fluid Flow in the Shallow Crust. A.G.U. Monograph, vol. 113, pp. 27–49.
Izett, G.A., Obradovich, J.D., 1994. $^{40}Ar/^{39}Ar$ age constraints for the Jaramillo Normal Subchron and the Matuyama-Brunhes geomagnetic boundary. Journal of Geophysical Research 99, 2925–2934.
Karlstrom, K.E., Cather, S.M., Kelley, S.A., Heizler, M.T., Pazzaglia, F.J., Roy, M., 1999. Sandia Mountains and Rio Grande Rift; ancestry of structures and history of deformation. New Mexico Geological Society Guidebook 50, 155–166.
Kamb, W.B., 1959. Ice petrofabric observations from Blue Glacier, Washington, in relation to theory and experiment. Journal of Geophysical Research 64, 1891–1909.
Kelley, V.C., 1979. Tectonics, middle Rio Grande Rift, New Mexico. In: Riecker, R.E. (Ed.), Rio Grande Rift: Tectonics and Magmatism, pp. 57–70.
Kelley, V.C., 1982. The right-relayed Rio Grande Rift, Taos to Hatch, New Mexico. New Mexico Geological Society Guidebook 33, 147–151.
Knipe, R.J., 1993. The influence of fault zone processes and diagenesis on fluid flow. AAPG Studies in Geology 36, 135–151.
Lachenbruch, A., 1962. Mechanics of thermal contraction cracks and ice-wedge polygons in permafrost. Geological Society of America Special Paper 70.
Lewis, C.J., Baldridge, W.S., 1994. Crustal extension in the Rio Grande Rift, New Mexico; half-grabens, accommodation zones, and shoulder uplifts in the Ladron Peak-Sierra Lucero area. Geological Society of America Special Paper 291, 135–155.
Lewis, C.J., Gardner, J.N., Schultz-Fellenz, E.S., Lavine, A., Reneau, S.L., Olig, S., 2009. Fault interaction and along-strike variation in throw in the Pajarito fault system, Rio Grande rift, New Mexico. Geosphere 5, 252–269.
Mauldon, M., Mauldon, J.G., 1997. Fracture sampling on a cylinder: from scan-lines to boreholes and tunnels. Rock Mechanics and Rock Engineering 30, 129–144.
Minor, S.A., Hudson, M.R., 2007. Regional survey of structural properties and cementation patterns of fault zones in the northern part of the Albuquerque Basin, New Mexico; implications for ground-water flow. U.S. Geological Survey Professional Paper, Report 1719.
Moon, V., 1993. Geotechnical characteristics of ignimbrite: a soft pyroclastic rock type. Engineering Geology 35, 33–48.
Myers, R., Aydin, A., 2004. The evolution of faults formed by shearing across joint zones in sandstone. Journal of Structural Geology 26, 947–966.
Olson, J.E., 1993. Joint pattern development: effects of subcritical crack growth and mechanical crack interaction. Journal of Geophysical Research 98, 12251–12265.
Olson, J., Pollard, D.D., 1989. Inferring paleostresses from natural fracture patterns: a new method. Geology 17, 345–348.
Peacock, D.C.P., Sanderson, D.J., 1992. Effects of layering and anisotropy on fault geometry. Journal of the Geological Society 149, 793–802.
Pollard, D.D., Segall, P., Delaney, P., 1982. Formation and interpretation of dilatant echelon cracks. Geological Society of America Bulletin 93, 1291–1303.
Pollard, D.D., Aydin, A., 1988. Progress in understanding jointing over the past century. Geological Society of America Bulletin 100, 1181–1204.
Pollard, D.D., Segall, P., 1987. Theoretical displacements and stresses near fractures in rock: With applications to faults, joints, veins, dikes and solution surfaces. In: Atkinson, B.K. (Ed.), Fracture Mechanics of Rock, pp. 277–349.
Quane, S.L., Russell, J.K., 2002. Rock strength as a metric of welding intensity in pyroclastic deposits. European Journal of Mineralogy 15, 855–864.
Rawling, G.C., Goodwin, L.B., Wilson, J., 2001. Internal architecture, permeability structure, and hydrologic significance of contrasting fault-zone types. Geology 29, 43–46.
Reneau, S.L., Vaniman, D.T., 1998. Fracture characteristics in a disposal pit on Mesita del Buey, Los Alamos National Laboratory. Los Alamos National Laboratory Report LA-13539-MS.
Ross, C.S., Smith, R.L., 1961. Ash-flow tuffs: their origin, geologic relations, and identification. U.S. Geological Survey Professional Paper 366.
Salyards, S.L., Ni, J.F., Aldrich, M.J., 1994. Variation in paleomagnetic rotations and kinematics of the north-central Rio Grande Rift, New Mexico. Geological Society of America Special Paper 291, 59–71.
Sanders, R.E., Heizler, M.T., Goodwin, L.B., 2006. $^{40}Ar/^{39}Ar$ thermochronology constraints on the timing and Proterozoic basement exhumation and fault ancestry, southern Sangre de Cristo Range, New Mexico. Geological Society of America Bulletin 118, 1489–1506.
Schultz, R.A., Li, Q., 1995. Uniaxial strength testing of nonwelded Calico Hills Tuff, Yucca Mountain, Nevada. Engineering Geology 40, 287–299.
Schultz, R.A., Siddharthan, R.V., 2005. A general framework for the occurrence and faulting of deformation bands in porous granular rocks. Tectonophysics 411, 1–18.
Schultz, R.A., Fossen, H., 2008. Terminology for structural discontinuities. American Association of the Petroleum Geologists Bulletin 92, 853–867.
Segall, P., 1984. Formation and growth of extensional fracture sets. Geological Society of America Bulletin 95, 454–462.
Segall, P., Pollard, D.D., 1983. Joint formation in granitic rock of the Sierra Nevada. Geological Society of America Bulletin 94, 563–575.
Shipton, Z.K., Cowie, P.A., 2001. Damage zone and slip-surface evolution over μm to km scales in high-porosity Navajo sandstone, Utah. Journal of Structural Geology 23, 1825–1844.
Shipton, Z.K., Soden, A.M., Kirkpatrick, J.D., Bright, A.M., Lunn, R.J., 2006. How thick is a fault? Fault displacement-thickness scaling revisited. Geophysical Monograph 170, 193–198.
Sigda, J., Goodwin, L., Mozley, P., Wilson, J., 1999. Permeability alteration in small-displacement faults in poorly lithified sediments, Rio Grand Rift, Central New Mexico. In: Haneberg, W., Mozley, P., Moore, J., Goodwin, L. (Eds.), Faults and Subsurface Fluid Flow in the Shallow Crust. A.G.U. Monograph, vol. 113, pp. 51–68.
Smith, R.L., Bailey, R.A., 1966. The Bandelier Tuff: a study of ash-flow eruption cycles from zoned magma chambers. Bulletin of Volcanology 29, 83–104.
Smith, R.L., Bailey, R.A., Ross, C.S., 1970. Geologic map of the Jemez Mountains, New Mexico. U.S. Geological Survey Miscellaneous Geologic Investigations Map I-571, Scale 1:125,000.
Spell, T.L., Kyle, P.R., Baker, J., 1996. Geochronology and geochemistry of the Cerro Toledo rhyolite. In: New Mexico Geological Society Guidebook, 47th Field Conference, Jemez Mountains Region 47, pp. 263–268.
Stimac, J., Hickmott, D., Abell, R., Larocque, A.C.L., Broxton, D., Gardner, J., Chipera, S., Wolff, J., Gauerke, E., 1996. Redistribution of Pb and other volatile trace metals during eruption, devitrification, and vapor-phase crystallization of the Bandelier Tuff, New Mexico. Journal of Volcanology and Geothermal Research 73, 245–266.
Terzaghi, R.D., 1965. Sources of error in joint surveys. Geotechnique 15, 287–304.
Vaniman, D., Wohletz, K., 1990. Results of geological mapping/fracture studies: TA-55 area. Los Alamos National Laboratory Seismic Hazards Program memo EES1-SH90-17.
Wilson, J.E., Goodwin, L.B., Lewis, C.J., 2003. Deformation bands in nonwelded ignimbrites: petrophysical controls on fault-zone deformation and evidence of preferential fluid flow. Geology 31, 837–840.
Wilson, J.E., 2004. Characteristics of Faults in Nonwelded Ignimbrites From the Pajarito Plateau and Implications for Fluid Flow. Ph.D. thesis, New Mexico Institute of Mining and Technology.
Wilson, J.E., Goodwin, L.B., Lewis, C., 2006. Diagensis of deformation-band faults: the record and mechanical consequences of vadose-zone flow and transport through the Bandelier Tuff, Los Alamos, NM. Journal of Geophysical Research 111, B09201. doi:10.1029/2005JB003892.
Wohletz, K.H., 1995. Measurement and analysis of rock fractures in the Tshirege member of the Bandelier Tuff along Los Alamos Canyon adjacent to technical area-21. In: Broxton, D.E., Eller, P.G. (Eds.), Earth Science Investigations for Environmental Restoration – Los Alamos National Laboratory Technical Area 21. Los Alamos National Laboratory Report LA-12934-MS, pp. 19–32.
Wohletz, K.H., 1996. Fracture characterization of the Bandelier Tuff in OU-1098 (TA-2 and TA-41). Los Alamos National Laboratory Report LA-12194-MS.
Wolff, H.A., Gardner, J.N., 1995. Is the Valles caldera entering a new cycle of activity? Geology 23, 411–414.

Wong, T.F., David, C., Zhu, W., 1997. The transition from brittle faulting to cataclastic flow in porous sandstone: mechanical deformation. Journal of Geophysical Research 102, 3009–3025.
Wong, T.F., Zhu, W., 1999. Brittle faulting and permeability evolution; hydromechanical measurement, microstructural observation, and network modeling. In: Haneberg, B.C., Mozley, P.S., Moore, J.C., Goodwin, L.B. (Eds.), Faults and Subsurface Fluid Flow in the Shallow Crust. Geophysical Monograph, 113, pp. 83–99.
Zhang, X., Sanderson, D.J., 1995. Anisotropic features of geometry and permeability in fractured rock masses. Engineering Geology 40, 65–75.
Zhang, X., Sanderson, D.J., 1996. Numerical modeling of the effects of fault slip on fluid flow around extensional faults. Journal of Structural Geology 18, 109–119.